Flexible Single-Crystal Silicon Nanomembrane Photonic Crystal Cavity

Xiaochuan Xu,[*,†,‡,#] Harish Subbaraman,[‡,#] Swapnajit Chakravarty,[‡] Amir Hosseini,[‡] John Covey,[†] Yalin Yu,[§] David Kwong,[†] Yang Zhang,[†] Wei-Cheng Lai,[†] Yi Zou,[†] Nanshu Lu,[§] and Ray T. Chen[*,†]

[†]Microelectronics Research Center, The University of Texas at Austin, 10100 Burnet Road, Bldg. 160, Austin, Texas 78758, United States, [‡]Omega Optics, Inc. 8500 Shoal Creek Drive, Bldg. 4, Suite 200, Austin, Texas 78757, United States, and [§]Department of Aerospace Engineering and Engineering Mechanics, Center for Mechanics of Solids, Structures and Materials, Texas Materials Institute, The University of Texas at Austin, Austin, Texas 78712, United States. [#]Authors X.X. and H.S. contributed equally to this work.

ABSTRACT Flexible inorganic electronic devices promise numerous applications, especially in fields that could not be covered satisfactorily by conventional rigid devices. Benefits on a similar scale are also foreseeable for silicon photonic components. However, the difficulty in transferring intricate silicon photonic devices has deterred widespread development. In this paper, we demonstrate a flexible single-crystal silicon nanomembrane photonic crystal microcavity through a bonding and substrate removal approach. The transferred cavity shows a quality factor of 2.2×10^4 and could be bent to a curvature of 5 mm radius without deteriorating the performance compared to its counterparts on rigid substrates. A thorough characterization of the device reveals that the resonant wavelength is a linear function of the bending-induced strain. The device also shows a curvature-independent sensitivity to the ambient index variation.

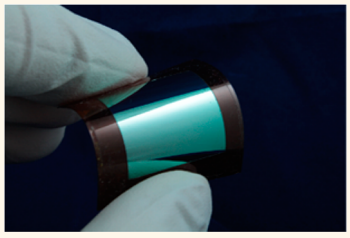

KEYWORDS: silicon nanomembrane · photonic crystal · photonic crystal cavity · flexible inorganic devices · wafer bonding

Developing flexible single-crystal silicon electronics and photonics is a modern instance of the archetypal human *versus* nature conflict. The enthusiasm of this effort is stimulated by a natural quandary: the well-established integrated electronics and photonics are manufactured on silicon-based substrates, which are rigid; on the contrary, all organisms are soft and curvilinear. This seemingly intrinsic incompatibility is resolved by the discovery that nanomembranes with thickness less than a few hundred nanometers can have flexural rigidities more than 15 orders of magnitude smaller than those of bulk wafers (>200 μm) of the same materials.[1,2] A hybrid platform which enjoys both the high performance of inorganic materials and the flexibility of organic materials is believed to have a vast range of unprecedented applications which could not be implemented by either inorganic or organic platforms alone. Since direct growth of single-crystal silicon on curvaceous and conformable organic surfaces is not possible, a hybrid platform is usually formed by physically transferring single-crystal silicon nanomembranes onto flexible plastic substrates.[3−16] Although still in its infancy, this hybrid approach has been extensively explored for applications in epidermal electronics,[3,13] implantable devices,[4,8,9] flexible silicon integrated circuits,[5,12,16] flexible solar cells,[10] bionic devices,[14] *etc.*

This hybrid platform also paves the way for flexible silicon photonics. Single-crystal silicon also has superior optical properties at telecommunication wavelengths, including a high refractive index and extremely low absorption loss, the likes of which cannot be obtained with organic materials. Having a high refractive index allows for sharp bends (of a few microns) without a significant increase in propagation loss.[17] As the bending radius of a flexible device is usually larger than a few millimeters, the loss introduced by the deformation itself is negligible compared to the scattering loss caused by surface roughness. This hybrid system also inherits the low absorption loss of single-crystal silicon. We have demonstrated stamp printing of single-crystal silicon nanomembrane-based multimode waveguides

* Address correspondence to xiaochuan.xu@utexas.edu, raychen@uts.cc.utexas.edu.

Received for review August 6, 2014 and accepted November 19, 2014.

Published online November 19, 2014
10.1021/nn504393j

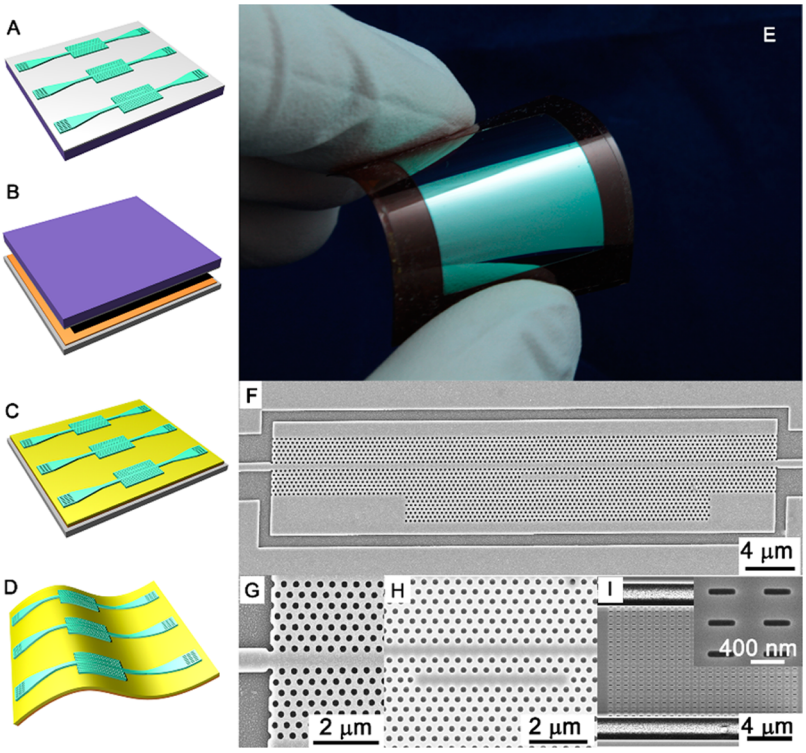

Figure 1. (A–D) Transfer process. (A) Pattern the photonic crystal microcavity on SOI. (B) Flip bond the SOI chip onto the polyimide film with SU-8 epoxy. (C) Remove the silicon handle and BOX layer with mechanical polishing, DRIE, and wet etching. (D) Peel off the polyimide film from the mechanical support. (E) Transferred 2 cm × 2 cm silicon nanomembrane on polyimide film. SEM image of (F) L13 photonic crystal microcavity, (G) input section of the photonic crystal waveguide, (H) magnified image of the transferred photonic crystal microcavity, and (I) SWG coupler.

onto polyimide films with a propagation loss of 1.1 dB/cm, which is comparable to the loss on a silicon-on-insulator (SOI) platform.[18] As usual, great opportunities are accompanied by great challenges. First, photonic devices are usually long in the longitudinal direction and short in the transverse direction, resulting in an aspect ratio exceeding a few thousand. This high aspect ratio cannot be accommodated by conventional stamp printing processes developed for flexible inorganic electronics. Moreover, the performance of photonic devices heavily relies on the integrity of its geometry with limited tolerance to geometrical defects. Although the stamp printing procedure does not have intrinsic limitations, the "peeling" and "printing" operations are more likely to generate geometrical defects due to engineering issues. This paper introduces a viable high yield transfer method, with which we demonstrate a flexible crystalline silicon photonic crystal microcavity which could be bent to a curvature of 5 mm radius, without any appreciable optical loss. The device's potential as a deformable sensor is also explored.

RESULTS AND DISCUSSION

Figure 1A–D briefly depicts the transfer sequence. A detailed description can be found in the Supporting Information. As shown in Figure 1A, the photonic devices are patterned on a 2 cm × 2 cm silicon-on-insulator (Soitec SOI) chip with a 250 nm single-crystal silicon layer, 3 μm buried oxide layer (BOX), and a 675 μm silicon handle using electron beam lithography and reactive ion etching (HBr/Cl_2). The patterned chip is flipped over and bonded onto a 125 μm thick polyimide substrate (Dupont Kapton HN) through adhesive bonding with SU-8 (Microchem) (Figure 1B). The native oxide on the SOI chip is removed by 1:6 buffered oxide etchant prior to bonding because the adhesion between SU-8 and SiO_2 is weak. Prior to bonding, the polyimide film is mounted on a rigid substrate. SU-8 is spin-coated on both the polyimide film and the SOI chip, both of which are baked at 65 °C for an extended period of time to improve surface quality as SU-8 has impressive self-planarization capability when heated above its glass transition temperature.[19,20] The SU-8 layer on the polyimide film is partially exposed to generate Lewis acid, which initiates cross-linking when the unexposed SU-8 on SOI is brought in contact. The pressure is applied by a homemade bonder, which is shown in Figure S3. After bonding, the silicon handle is removed by mechanical polishing followed by deep reactive ion etching (DRIE), as shown in Figure 1C. The DRIE process is tailored to reduce the processing temperature. The etch rate is about 2.7 μm/cycle with a selectivity of 80:1 to silicon dioxide (SiO_2), making the 3 μm thick BOX an excellent etch stop layer, which is then removed by concentrated 49% hydrofluoric acid. Finally, the

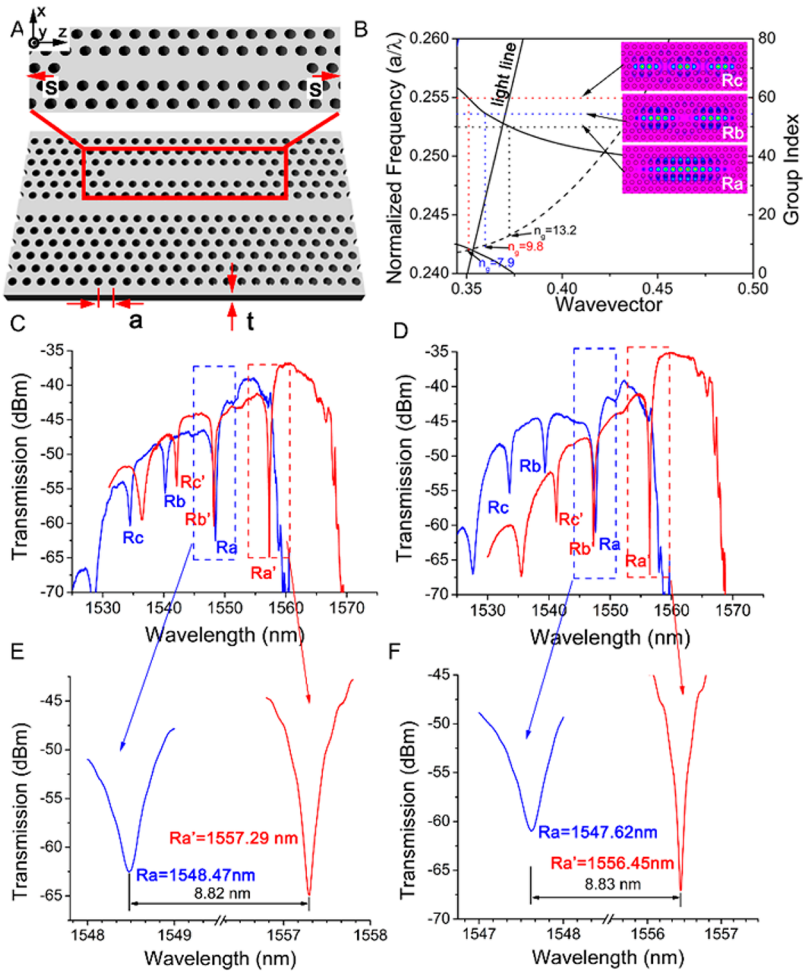

Figure 2. (A) Schematic of the L13 cavity. (B) Band diagram of the PCW (solid black curve). The L13 cavity resonance frequencies are indicated by dotted lines. Inset: $|H_y|^2$ of the three resonant modes. (C) Transmission spectra of the L13 PC microcavity device on SOI with deionized (DI) water as the top cladding (blue) and with glycerol as the top cladding (red). (D) Transmission spectra of the L13 PC microcavity device on polyimide film with DI water as the top cladding (blue) and with glycerol as the top cladding (red). (E) Zoomed-in image showing resonance R_a on SOI device with different top claddings. (F) Zoomed-in image showing resonance R_a on transferred device with different top claddings. Resonance wavelengths are also indicated in the figures.

polyimide film containing the silicon nanomembrane devices is peeled up from the rigid carrier (Figure 1D). Figure 1E shows the transferred 2 cm × 2 cm silicon nanomembrane. Figure S4 demonstrates that the film could be bent to a small curvature. The advantages of adhesive bonding include relatively low bonding temperatures, insensitivity to the bonding surface topology, and the ability to join virtually any two materials together. During the transfer procedure, SU-8 completely fills the holes and trenches in and around the photonic devices, providing mechanical support and protecting the delicate devices from mechanical failure. After transfer, oxygen plasma may be used to remove the SU-8 inside the holes for applications that require exposing the optical field to the outside world. Figure 1F–I shows the scanning electron microscope (SEM) images of the transferred L13 photonic crystal microcavity (Figure 1F–H) and the subwavelength grating (SWG) couplers (Figure 1I. Movie S1 in the Supporting Information shows that the film can bend, twist, and consistently return to its original form. It could also be cut as easily as a piece of paper.

Figure 2A illustrates the structure of the L13 photonic crystal microcavity comprising a linear photonic crystal microcavity side-coupled with a W1 photonic crystal waveguide (PCW). The cavity, which is formed by removing 13 holes along the Γ–K direction, is located two rows away from the W1 waveguide. The two holes at the two ends of the cavity are moved outward by a distance $s = 0.15a$ to reduce radiation loss and increase the quality factor (Q).[21] This optimized hole displacement is selected by experimentally comparing the Q of cavities with different hole shift.[21] The W1 PCW is formed by removing one row of holes along the Γ–K direction. The lattice constant a equals 393 nm in this work. The hole radius r is 108 nm, giving a r/a of 0.275. The thickness of the silicon slab t is 250 nm. An eight-period photonic crystal adiabatic taper is designed to improve the coupling efficiency between the strip waveguide and the PCW.[22] The

dispersion relation of the W1 PCW (solid curve) is simulated by three-dimensional plane wave expansion, as shown in Figure 2B. The resonance frequencies are also indicated by the dotted lines. The $|H_y|^2$ distribution of the resonant modes are shown in the inset of Figure 2B. Among the three resonances, resonances R_b and R_c are above the SiO_2 light line ($n \sim 1.45$ at 1550 nm), resulting in higher radiation loss and lower Q. Resonance R_a is of the most interest not only because of its high Q, but also because of its higher group index ($n_g \sim 13.2$), which provides greater interaction between the slowly traveling photons and analytes compared to a strip waveguide. For device characterization, SWGs are designed and integrated to couple light in and out of the transferred devices.[23] The transmission spectrum is obtained by analyzing the light coupled out from SWG with an optical spectral analyzer (OSA). The transmission spectra of the L13 cavity with water ($n \sim 1.33$ at 1550 nm) as its top cladding before and after being transferred to a new substrate are shown by the blue curves in Figure 2C,D. The presence of water, which is highly absorptive in the near-infrared wavelength range (absorbance: $\alpha \sim 800\ m^{-1}$ at 1550 nm), increases the absorption loss and lowers the Q to 9×10^3. After transfer, resonance R_a (1548.47 nm) blue shifts to 1547.62 nm, while the quality factor remains unchanged. The blue shift of resonances is due to the expansion of the holes induced by the transfer process. To determine the bulk sensitivity of the device, glycerol ($n \sim 1.46$ at 1550 nm) is dropped on top of the microcavity, and the transmission spectra from the devices on SOI and on polyimide are measured again, as indicated by the red curves in Figure 2C,D, respectively. The Q factor increases to 2.2×10^4 because glycerol is transparent in the wavelength range of interest. The resonance shift induced by the refractive index change of the top cladding is 8.82 nm, corresponding to a sensitivity of 68 nm/RIU (refractive index unit), which is comparable to the devices demonstrated on rigid SOI platforms.[24−26]

The bending characteristics of the flexible photonic crystal microcavity are investigated with the measurement setup shown in Figure 3. The two ends of the sample are constrained on the jaws of a caliper but allowed to rotate freely. The specimen is buckled upward or downward by sliding the movable jaw inward. The system allows the distance between the two jaws to be controlled with an accuracy better than 0.1 mm. Light is also coupled *via* single mode fibers into and out of the device through SWGs. The SWGs have been designed to have repeatable performance on curvatures with different bending radii. A detailed description of the SWGs is provided in the Supporting Information. The bending shape of the specimen can be approximated by a sinusoidal function (eq S3). The bending radius at the peak of the curvature is estimated by the second derivative of the sinusoidal curve,

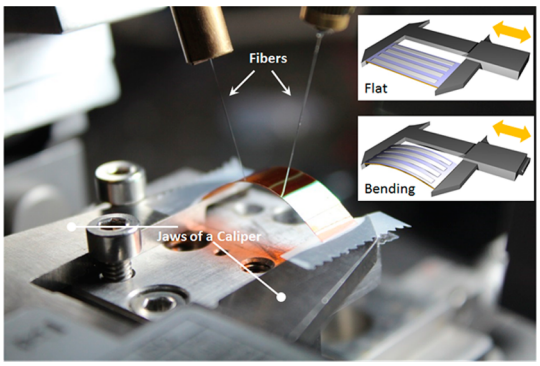

Figure 3. Configuration of the bending experiment. Inset: Sliding the movable jaws will buckle the specimen upward or downward.

as shown in eq S5.[27] We investigated four different types of axial bending: longitudinal face-out bending (LFO), longitudinal face-in bending (LFI), transverse face-out bending (TFO), and transverse face-in bending (TFI). For longitudinal bending, the bending direction is parallel to the light propagation direction (z axis), while it is perpendicular for transverse bending (x axis). In face-out bending (bending radius $R > 0$), the silicon nanomembrane experiences tensile stress in the bending direction, and in face-in bending ($R < 0$), it experiences compressive stress in the bending direction. The strain γ_{bend} of the silicon nanomembrane in the bending direction equals the distance from the neutral surface, d_n, divided by the bending radius R. The absolute value of R is between infinity (flat) and 5 mm. The corresponding absolute value of the strain $|\gamma_{bend}|$ in the bending direction is between 0 and 1.2%, as indicated in Figure S9. The experimentally observed shifts of resonance 1 in LFO, LFI, TFO, and TFI bending are shown by the red dots in Figure 4A−D, respectively. The resonance shifts to longer wavelength when the specimen is under tensile strain ($\gamma_{bend} > 0$) and to shorter wavelength when it is under compressive strain ($\gamma_{bend} < 0$). The strain sensitivity is summarized in Table 1. The resonant shift exhibits a linear correlation with strain. The sensitivities for LFO, LFI, TFO, and TFI are 0.673, 0.656, 0.588, and 0.591 pm/$\mu\varepsilon$, respectively, as calculated by linear regression. The device is observed to be slightly more sensitive to longitudinal bending than transverse bending.

The effects of bending are 2-fold: distort the geometry and transform the isotropic refractive index tensor into anisotropic. Geometrical distortion includes turning the circular holes into elliptical holes, changing the lattice structure, and altering the cavity properties. As the hexagonal lattice is distorted into a pseudohexagonal lattice, the hexagonal symmetry in the reciprocal lattice is broken and the irreducible Brillouin zone splits into three, shifting the photonic band gap structure and the guided mode, as shown qualitatively in the insets in Figure 4A−D.[28] Because of the asymmetry of the device, as implied in Figure 1F, the deformation

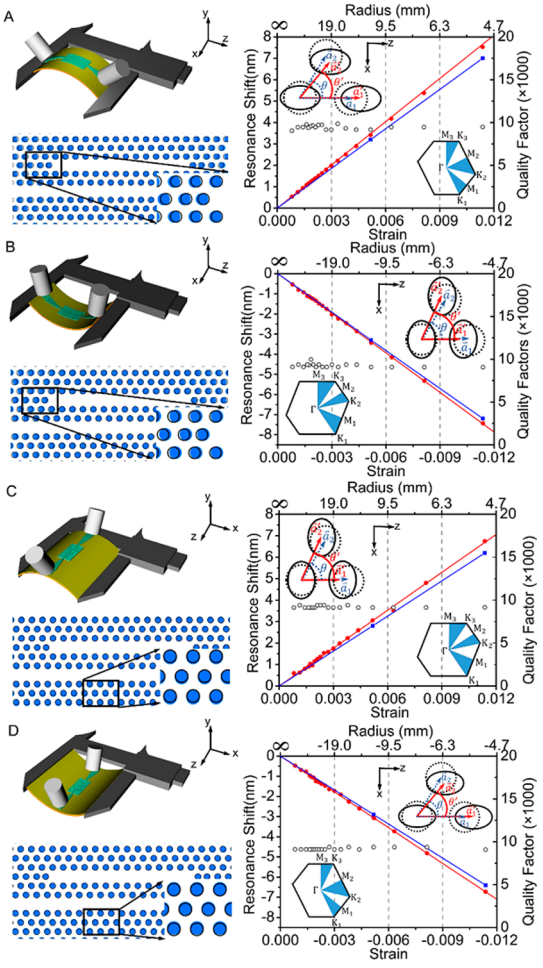

Figure 4. Bending characteristics of the transferred L13 PC microcavity under (A) LFO bending, (B) LFI bending, (C) TFO bending, and (D) TFI bending. The top left insets are the schematics depicting the bending configurations. The bottom left insets show the deformed geometries generated by FEM simulations. The right figures show the experimental (red) and simulation (blue) correlation between resonance R_a wavelength shift and strain. The insets in the right figures show the deformation of the holes and the corresponding distortion of the reciprocal lattice. The small black circles are the measured quality factors of the cavity at different bending radii.

TABLE 1. Strain Sensitivity (pm/$\mu\varepsilon$)

	LFO	LFI	TFO	TFI
experiment	0.673	0.656	0.588	0.591
simulation	0.616	0.633	0.545	0.563

is not symmetric either. Therefore, to give a precise account of the deformation, the whole device is simulated with finite element method (FEM) by prescribing corresponding displacements on the boundary. Since the dimension of the photonic crystal microcavity (10 μm × 40 μm) is much smaller than the minimum bending radius (5 mm), the strain could be closely approximated by in-plane uniaxial strain. The simulated deformed geometries are shown in the bottom left insets in Figure 4A–D, which show the deformation

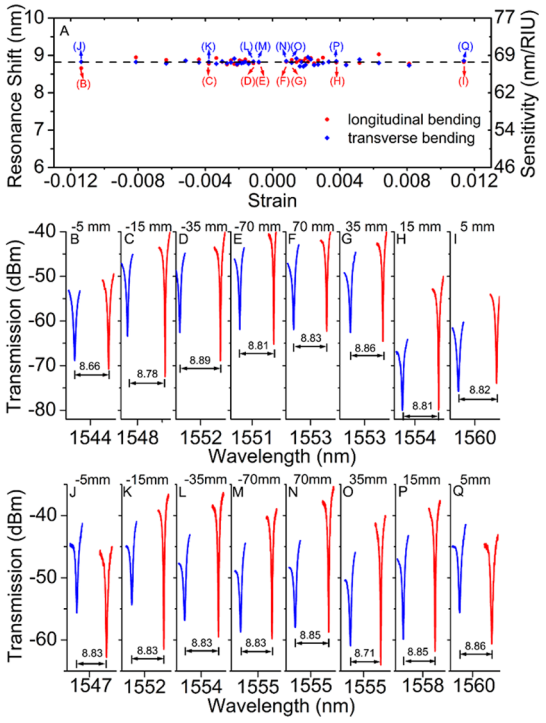

Figure 5. (A) Resonance shift caused by analytes with different refractive indices. A drop of analyte can be clearly seen adhering the surface even under bent conditions. (B-Q) Transmission spectra of resonance R_a in different bending cases: (B–E) LFO; (F–I) LFI; (J–M) TFO; (N–Q) TFI. For each bending case, four different bending radii are selected due to the limited space, including 5, 15, 35, and 70 mm. Blue curve: water top cladding. Red curve: glycerol top cladding.

and relocation of the holes. The L13 cavity is also altered by strain, leading to the change of its resonance property. As an example, the cavity is elongated under LFO bending, while its width shrinks due to Poisson's effect. In addition to the geometry distortion, the photoelastic effect also causes significant resonance shift. The relation between the components of the refractive index tensor and the stress can be calculated by eqs S9–S21. Due to the complexity of the structure, the exact calculation of stress as a function of position is prohibitive; thus, an averaged value is therefore adopted to estimate the refractive index tensor. The results are shown in Figure S9. Take LFO bending again as an example, n_{zz} increases while n_{xx} and n_{yy} decrease with increasing tensile strain. The deformed geometry and the refractive index tensors are used as input for finite-difference time-domain (FDTD) simulations. As the slab photonic crystal does not support pure transverse electric modes, all components of the refractive index tensor need to be considered in the FDTD simulations. The simulated resonance shift is shown by the blue lines in Figure 4A–D, which matches the experimental results with a discrepancy around 10%, possibly caused by errors induced due to approximations and utilizing the averaged stress values in the simulations. Another interesting phenomenon that has been observed is the Q of resonance R_a remains around

9×10^3 under different bending conditions due to the high index contrast between silicon and its cladding materials, as indicated by the black circles in Figure 4A–D.

As aforementioned, ultrathin monocrystalline devices are expected to not only exhibit excellent flexibility but also show comparable performance to their rigid counterparts. For a flexible and conformal photonic sensor, it would be even more valuable if its sensitivity is independent of the bending radius. To determine the effect of bending on sensitivity, measurements are performed with water and glycerol, just like the previous discussion. The results are summarized in Figure 5. A number of different bending radii have been investigated, and the results are summarized in Figure 5A. The device exhibits an average sensitivity of 68 nm/RIU under different bending conditions, which is identical to the sensitivity when the specimen lies flat. Four different bending radii (5, 15, 35, and 70 mm) are plotted in Figure 5B–Q for each bending configuration. The bending could delocalize the resonant mode field into the cladding and subsequently affect the sensitivity. In the face-out bending, for instance, the resonant mode field tends to delocalize into the top cladding. The overlap factor increases as the bending radius reduces, and thus the sensitivity could increase. Due to the relatively large bending radii and small strain, this phenomenon is negligible. The results also imply that the flexible photonic crystal microcavity can be reliably used on a curved surface.

CONCLUSION

We have demonstrated a flexible monocrystalline photonic crystal microcavity sensor using a bonding and silicon handle removal-based transfer technique. The demonstrated photonic crystal microcavity shows a quality factor up to 2.2×10^4. The high-performance sensor device could bend to a curvature of 5 mm radius without deteriorating the quality factor. The resonant wavelength shift is linearly correlated to the uniaxial strain. As a refractive index sensor, the flexible cavity demonstrates a deformation-independent sensitivity, which is crucial for real applications. This effort proves the feasibility of achieving intricate high-quality photonic devices on plastic substrates.

METHODS

Device Fabrication. The device is fabricated on commercially available silicon-on-insulator with 250 nm single-crystal silicon device layer, 3 μm buried oxide layer, and 675 μm silicon handle. The wafer is cleaved into 2 cm $\times$ 2 cm chips, and the chips are cleaned through a piranha bath. Hexamethyldisilazane is spin-coated at 4000 rpm for 35 s to enhance the adhesion between the electron beam resist and silicon. Electron beam resist ZEP520a is spin-coated at 6000 rpm for 35 s, giving a resist of 350 nm thickness. The pattern is transferred onto the resist by JBL 6000 and then to the silicon layer through reactive ion etching (HBr/Cl_2). The resist is stripped off by PG remover and a piranha bath.

Measurements. The bending tests are carried out by mounting the samples between the jaws of a Vernier caliper,[29] as illustrated in Figure 3 and its insets. The specimen is bent to a sinusoidal shape under a uniaxial compressive displacement applied by the movable jaw. Both ends of the specimen are linked to the jaws *via* Scotch tape but allowed to rotate almost freely in the vertical direction. This configuration can be approximated by the mechanical model of simply supported beams.[30] When the film is bent upward, it is defined as face-out bending and the silicon nanomembrane is subjected to a tensile stress. In contrast, as the film is bent downward, it is defined as face-in bending and the silicon nanomembrane is subjected to a compressive stress.[31] The study is performed on the specimen with an initial length of L. After applying a compressive displacement ΔL by the movable jaw, the specimen buckles and bends to an end-to-end length of $L - \Delta L$. ΔL can be measured by a caliper with an accuracy of 0.01 mm.

Light is coupled into devices through SWGs. A detailed discussion on SWGs is available in the Supporting Information. To characterize the devices, light from a broad-band source is polarized by a free space polarizer and delivered by a polarization maintaining fiber. The light from the output grating is harvested by a conventional single-mode fiber (SMF28) and analyzed by an OSA. Both the input and output fibers are held by copper tubes, which are mounted on 10° wedges sitting on *xyz* stages.

Conflict of Interest: The authors declare no competing financial interest.

Acknowledgment. The author would like to acknowledge Prof. J. Rogers at the University of Illinois at Urbana—Champaign for productive discussion. This research was funded by the Air Force Office of Scientific Research (AFOSR) Multidisciplinary University Research Initiative (MURI) under contract No. FA9550-08-1-0394 and Small Business Technology Transfer (STTR) under contract No. FA9550-11-C-0014 (program manager: Dr. G. Pomrenke), and by the National Institutes of Health (NIH) under contract No. HHSN2612012-00043C.

Supporting Information Available: Details of the fabrication process, grating coupler design and testing, mechanic analysis, and a video showing the flexible cavity. This material is available free of charge *via* the Internet at http://pubs.acs.org.

REFERENCES AND NOTES

1. Rogers, J. A.; Lagally, M. G.; Nuzzo, R. G. Synthesis, Assembly and Applications of Semiconductor Nanomembranes. *Nature* **2011**, *477*, 45–53.
2. Cavallo, F.; Lagally, M. G. Semiconductors Turn Soft: Inorganic Nanomembranes. *Soft Matter* **2010**, *6*, 439–455.
3. Huang, X.; Yeo, W. H.; Liu, Y. H.; Rogers, J. A. Epidermal Differential Impedance Sensor for Conformal Skin Hydration Monitoring. *Biointerphases* **2012**, *7*, 1–9.
4. Hwang, S. W.; Tao, H.; Kim, D. H.; Cheng, H. Y.; Song, J. K.; Rill, E.; Brenckle, M. A.; Panilaitis, B.; Won, S. M.; Kim, Y. S.; *et al.* A Physically Transient Form of Silicon Electronics. *Science* **2012**, *337*, 1640–1644.
5. Kim, D. H.; Ahn, J. H.; Choi, W. M.; Kim, H. S.; Kim, T. H.; Song, J. Z.; Huang, Y. G. Y.; Liu, Z. J.; Lu, C.; Rogers, J. A. Stretchable and Foldable Silicon Integrated Circuits. *Science* **2008**, *320*, 507–511.
6. Meitl, M. A.; Zhu, Z. T.; Kumar, V.; Lee, K. J.; Feng, X.; Huang, Y. Y.; Adesida, I.; Nuzzo, R. G.; Rogers, J. A. Transfer Printing by Kinetic Control of Adhesion to an Elastomeric Stamp. *Nat. Mater.* **2006**, *5*, 33–38.
7. Ying, M.; Bonifas, A. P.; Lu, N. S.; Su, Y. W.; Li, R.; Cheng, H. Y.; Ameen, A.; Huang, Y. G.; Rogers, J. A. Silicon Nanomembranes for Fingertip Electronics. *Nanotechnology* **2012**, *23*, 1–7.

8. Kim, R. H.; Tao, H.; Kim, T. I.; Zhang, Y. H.; Kim, S.; Panilaitis, B.; Yang, M. M.; Kim, D. H.; Jung, Y. H.; Kim, B. H.; *et al.* Materials and Designs for Wirelessly Powered Implantable Light-Emitting Systems. *Small* **2012**, *8*, 2812–2818.
9. Kim, D. H.; Ghaffari, R.; Lu, N. S.; Rogers, J. A. Flexible and Stretchable Electronics for Biointegrated Devices. *Annu. Rev. Biomed. Eng.* **2012**, *14*, 113–128.
10. Yoon, J.; Baca, A. J.; Park, S. I.; Elvikis, P.; Geddes, J. B.; Li, L. F.; Kim, R. H.; Xiao, J. L.; Wang, S. D.; Kim, T. H.; *et al.* Ultrathin Silicon Solar Microcells for Semitransparent, Mechanically Flexible and Microconcentrator Module Designs. *Nat. Mater.* **2008**, *7*, 907–915.
11. Park, S. I.; Xiong, Y. J.; Kim, R. H.; Elvikis, P.; Meitl, M.; Kim, D. H.; Wu, J.; Yoon, J.; Yu, C. J.; Liu, Z. J.; *et al.* Printed Assemblies of Inorganic Light-Emitting Diodes for Deformable and Semitransparent Displays. *Science* **2009**, *325*, 977–981.
12. Rogers, J. A.; Someya, T.; Huang, Y. G. Materials and Mechanics for Stretchable Electronics. *Science* **2010**, *327*, 1603–1607.
13. Kim, D. H.; Lu, N. S.; Ma, R.; Kim, Y. S.; Kim, R. H.; Wang, S. D.; Wu, J.; Won, S. M.; Tao, H.; Islam, A.; *et al.* Epidermal Electronics. *Science* **2011**, *333*, 838–843.
14. Song, Y. M.; Xie, Y. Z.; Malyarchuk, V.; Xiao, J. L.; Jung, I.; Choi, K. J.; Liu, Z. J.; Park, H.; Lu, C. F.; Kim, R. H.; *et al.* Digital Cameras with Designs Inspired by the Arthropod Eye. *Nature* **2013**, *497*, 95–99.
15. Ma, Z. Q.; Zhang, K.; Seo, J. H.; Zhou, H.; Sun, L.; Yuan, H. C.; Qin, G. X.; Pang, H. Q.; Zhou, W. D. Fast Flexible Electronics Based on Printable Thin Mono-crystalline Silicon. *ECS Trans.* **2011**, *34*, 137–142.
16. Zhou, H.; Seo, J. H.; Paskiewicz, D. M.; Zhu, Y.; Celler, G. K.; Voyles, P. M.; Zhou, W. D.; Lagally, M. G.; Ma, Z. Q. Fast Flexible Electronics with Strained Silicon Nanomembranes. *Sci. Rep.* **2013**, *3*, 1291.
17. Vlasov, Y. A.; McNab, S. J. Losses in Single-Mode Silicon-on-Insulator Strip Waveguides and Bends. *Opt. Express* **2004**, *12*, 1622–1631.
18. Xu, X. C.; Subbaraman, H.; Hosseini, A.; Lin, C. Y.; Kwong, D.; Chen, R. T. Stamp Printing of Silicon-Nanomembrane-Based Photonic Devices onto Flexible Substrates with a Suspended Configuration. *Opt. Lett.* **2012**, *37*, 1020–1022.
19. Stephan, K.; Gabriela, B.; Michael, L.; Daniel, H.; Anja, B. Processing of Thin SU-8 Films. *J. Micromech. Microeng.* **2008**, *18*, 125020.
20. Santeri, T.; Sami, F. Wafer-Level Bonding of MEMS Structures with SU-8 Epoxy Photoresist. *Phys. Scr., T* **2004**, *114*, 223–226.
21. Akahane, Y.; Asano, T.; Song, B. S.; Noda, S. High-*Q* Photonic Nanocavity in a Two-Dimensional Photonic Crystal. *Nature* **2003**, *425*, 944–947.
22. Johnson, S. G.; Bienstman, P.; Skorobogatiy, M. A.; Ibanescu, M.; Lidorikis, E.; Joannopoulos, J. D. Adiabatic Theorem and Continuous Coupled-Mode Theory for Efficient Taper Transitions in Photonic Crystals. *Phys. Rev. E* **2002**, *66*, 066608.
23. Xu, X. C.; Subbaraman, H.; Covey, J.; Kwong, D.; Hosseini, A.; Chen, R. T. Complementary Metal-Oxide-Semiconductor Compatible High Efficiency Subwavelength Grating Couplers for Silicon Integrated Photonics. *Appl. Phys. Lett.* **2012**, *101*, 031109.
24. Lai, W. C.; Chakravarty, S.; Zou, Y.; Chen, R. T. Silicon Nanomembrane Based Photonic Crystal Microcavities for High Sensitivity Bio-sensing. *Opt. Lett.* **2012**, *37*, 1208–1210.
25. Pal, S.; Guillermain, E.; Sriram, R.; Miller, B. L.; Fauchet, P. M. Silicon Photonic Crystal Nanocavity-Coupled Waveguides for Error-Corrected Optical Biosensing. *Biosens. Bioelectron.* **2011**, *26*, 4024–4031.
26. Yi, Z.; Chakravarty, S.; Kwong, D. N.; Wei-Cheng, L.; Xiaochuan, X.; Xiaohui, L.; Hosseini, A.; Chen, R. T. Cavity-Waveguide Coupling Engineered High Sensitivity Silicon Photonic Crystal Microcavity Biosensors with High Yield. *IEEE J. Sel. Top. Quantum Electron.* **2014**, *20*, 1–10.
27. Park, S. I.; Ahn, J. H.; Feng, X.; Wang, S. D.; Huang, Y. G.; Rogers, J. A. Theoretical and Experimental Studies of Bending of Inorganic Electronic Materials on Plastic Substrates. *Adv. Funct. Mater.* **2008**, *18*, 2673–2684.
28. Kim, S.; Gopalan, V. Strain-Tunable Photonic Band Gap Crystals. *Appl. Phys. Lett.* **2001**, *78*, 3015–3017.
29. Park, S.; Wang, G.; Cho, B.; Kim, Y.; Song, S.; Ji, Y.; Yoon, M. H.; Lee, T. Flexible Molecular-Scale Electronic Devices. *Nat. Nanotechnol.* **2012**, *7*, 438–442.
30. Timoshenko, S. P.; Gere, J. M. *Theory of Elastic Stability*, 2nd ed.; Dover Publications: Mineola, NY, 2009.
31. Ni, J. L.; Zhu, X. F.; Pei, Z. L.; Gong, J.; Sun, C.; Zhang, G. P. Comparative Investigation of Fracture Behaviour of Aluminium-Doped ZnO Films on a Flexible Substrate. *J. Phys. D: Appl. Phys.* **2009**, *42*, 175404.

Supplementary Materials for

Flexible Single Crystal Silicon Nanomembrane Photonic Crystal Cavity

Xiaochuan Xu,[1,2,, ‡] Harish Subbaraman,[2, ‡] Swapnajit Chakravarty,[2] Amir Hosseini,[2] John Covey,[1] Yalin Yu,[3] David Kwong,[1] Yang Zhang,[1] Wei-Cheng Lai,[1] Yi Zou,[1] Nanshu Lu,[3] and Ray T. Chen[1,*]*

correspondence to: xiaochuan.xu@utexas.edu
raychen@uts.cc.utexas.edu

This PDF file includes:

Materials and Methods
Figure S1 to S10
Table S1
Caption for Movie S1

Other Supplementary Materials for this manuscript includes the following:

Movie S1

Materials and Methods

1. Device Fabrication

The device is fabricated on commercially available silicon-on-insulator (SOI) with 250 nm single crystal silicon device layer, 3 μm buried oxide (BOX) layer, and 675 μm silicon handle, as shown in Figure S1a. The wafer is cleaved into 2 cm×2 cm chips, and the chips are cleaned through piranha bath. Hexamethyldisilazane (HMDS) is spin coated at 4000 rpm for 35s to enhance the adhesion between electron beam resist and silicon. Electron beam resist ZEP520a is spin coated at 6000 rpm for 35s, giving a resist of 350 nm thickness. The pattern is transferred onto the resist by JBL 6000 (Figure S1b), and then to the silicon layer through reactive ion etching (HBr/Cl_2), as shown in Figure S1c. The resist is stripped off by PG remover and piranha bath.

2. Transfer Procedure

The transfer process is illustrated in Figure S2. As shown in Figure S2a, the Kapton film is cleaned with acetone and methanol, and dried with compressed nitrogen gas. To make chip handling and bonding easier, the Kapton film is mounted on a rigid substrate, such as a silicon chip. A layer of 2 μm thick SU-8 is spin casted on the Kapton film and baked at 90°C for 20 minutes. The SOI chip with fabricated L13 cavities is cleaned by piranha bath. The native oxide is removed by 1:6 buffered oxide etchant (BOE). A layer of 2 μm SU-8 is spin coated and also baked at 90°C for 20 minutes. The extended baking time assures a complete evaporation of the solvent, which is crucial to a successful bonding. Besides, SU-8 has extraordinary self-planarization capability at a temperature above its glass transition temperature (64 °C), [1, 2] and thus long term baking minimizes the edge bead effect as well as other thickness variations.[2]

SU-8 is an acid-catalyzed polymer.[3] Its crosslink relies on the generation of Lewis acid through ultra-violet (UV) exposure. Since neither Kapton nor SOI is transparent to UV light, it is impossible to cure SU-8 after bonding. The conventional bonding procedure is to cure SU-8 prior to bonding and let it reflow above its glass transition temperature, which is around 180 °C, depending on its crosslink level. However, since silicon, SU-8, and Kapton have distinct coefficients of thermal expansion (CTE), the stack could crack during the thermal cycle involving high temperature. SU-8 is a chemical amplified resist. One photon produces a photoproduct that in turn induces hundreds of reactions. Therefore, the SU-8 layer on Kapton is partially cured before bonding, while the SU-8 on SOI remains uncured. The partially cured SU-8 provides Lewis acid to initiate crosslinking and the uncured SU-8 serves as a buffer layer, which reflows at low temperature. The bonding pressure is applied through a home-made bonder (Figure S3). The sample is mounted between two thick Pyrex glass slides. The steel ball and the Belleville washer spreads the point force generated by the thumb screw onto the thick Pyrex glass plate. This structure forms a gradient pressure distribution with higher pressure at the center and lower at the edges. This distribution prevents the formation of air cavities in between the two SU-8 layers. The applied pressure reduces as SU-8 reflows, which can be compensated by the thermal expansion of the Belleville washers. The sample is kept in a 90 °C oven for 12 hours to allow for polymer to reflow and to squeeze out the trapped air bubbles.

After bonding, the silicon handle is removed by deep reactive ion etch (DRIE), as described in Figs. S2c and S2d. DRIE generates a large amount of heat, so the carrier wafer on which the sample sits is kept at ~ 15 °C through Helium flow underneath. However, the thermal conductivities of SU-8 and Kapton are merely 0.2 W/mK and 0.52 W/mK, respectively, and thus the heat generated by the etching process cannot be dissipated fast enough. Consequently, a significant temperature gradient builds up between the top surface and the bottom of the rigid

substrate, subjecting the sample to cracking. The CTE mismatch further aggravates this issue. To control the thermal budget, the silicon handle is mechanically polished to ~100 μm, as shown in Figure S2c, to shorten the etching time. The etching recipe is also carefully optimized to accommodate the thermal requirements. The conventional Bosch process contains three steps: polymer deposition, polymer etching, and silicon etching. The polymer deposition time is set to 5s to protect the perimeter of the membrane, because the charges accumulated on the Kapton surface bend the electric field and etch silicon and SU-8 from the side. As the quality of the perimeter of silicon nanomembrane is not important, the anisotropic polymer etching step is removed in this application. The polymer is removed during the silicon etching step. The inductively coupled plasma (ICP) power is carefully tuned to keep it slightly above the threshold of maintaining plasma to reduce heat generation. This adjustment sacrifices the etch rate. To compensate it, a long silicon etching time of 30s is used in each cycle. The etch rate of this recipe is around 2.7 μm/cycle with a selectivity of ~80:1 over silicon dioxide. The 3 μm BOX is therefore used as a stopping layer to protect the SiNM underneath, and it can be removed by hydrofluoric (HF) acid etching afterwards.

Before removing the BOX layer, photoresist is applied on both the bottom and the top of the sample except the BOX region for protection. Because HF attacks Kapton/SU-8 bonds and SU-8/silicon bonds, a few droplets of HF are applied on the BOX directly instead of immersing the whole sample into HF solution to prevent the delamination of the silicon nanomembrane. The surface tension of the silicon dioxide constrains the solution within the SiNM. The drawback is that etching speed decreases as the HF concentration decreases. Thus, a few more drops of HF needs to be added to maintain sufficient HF concentration. The process is shown in Figure S2e. After transfer, the thickness of the SU-8 is measured to be around 3 μm. The thickness variation across the entire chip is ~200 nm, due to gradient bonding pressure. The holes of the photonic crystal structures are filled with SU-8 which reduces the sensitivity of the photonic crystal cavity. Another reactive ion etching step is used to remove the SU-8 inside the holes, as shown in Figure S2f. Finally, the Kapton film is peeled off from the silicon carrier, as shown in Figure S2g. The sample after transfer is shown in Figure S4. It can be seen that the transferred devices can be bent beyond the limit of their rigid counterparts without breaking or cracking.

3. Grating Coupler Design and Characterization

Coupling light into and out from the transferred devices is very challenging. End-fire coupling is a straight forward option but not a feasible one for flexible silicon photonic devices. First the facet is extremely difficult to prepare due to the soft nature of the substrate, [4] which turns the simple solution into a disaster. Moreover, the coupling efficiency is close to zero via direct butt coupling due to the large mode mismatch. An alternative solution is grating couplers. However, conventional grating couplers require multiple lithography and etching steps to reduce the index contrast and increase directionality.[5-7] Besides, the one dimension periodic structure is not mechanically strong enough for flexible devices. Subwavelength grating (SWG) couplers provide a viable option.[8, 9] The low index region of SWG couplers is comprised of artificial nanostructures, which are more robust. The entire grating can be fabricated together with other photonic components with efficiency comparable to those that demand multiple lithography and alignment steps.[5-7] Since the holes of SWG couplers could be completely filled or partially filled with SU-8, the grating coupler needs to work properly in both situations.

Figure 5a shows the schematic of the SWG coupler. A complete study of the SWG coupler requires three dimension (3D) simulations. The simulation time would be prohibitively long. To simplify the simulation, we treat the subwavelength structures as a uniform material because the

subwavelength period is much smaller than the wavelength inside the waveguide according to effective medium theory (EMT).[9-11] So the 3D problem can be simplified into 2D. In addition, the reflection of bottom cladding can be ignored because the SU-8 layer is very thick, and the index contrast between SU-8 (1.575) and Kapton (1.79) is much smaller than that between silicon dioxide (1.45) and silicon (3.476). The simulation and optimization procedure is similar to reference [8], so it would not be reiterated here. The optimized subwavelength refractive index $n_{sub}$is 2.45. The grating period Λ is 0.69 μm. An example of the fabricated grating coupler is shown in Figure S5b. The 2D finite-difference-time-domain (FDTD) simulation of fiber to grating coupling is shown by the red curve in Figure S5c. The coupling angle is ~9.4°. The grating has a theoretical coupling efficiency of -3.2 dB. The transmission spectrum of the grating coupler after transfer is shown in the same figure (blue curve). The grating coupler demonstrates a coupling efficiency of -4.4 dB at 1536.7 nm, and a 3 dB bandwidth of 50 nm. The discrepancy of the measured coupling efficiency and the peak wavelength from the simulated values is caused by the dimension variation induced by the transfer process. When the holes are infiltrated with SU-8, the refractive index of the subwavelength structure increases to 2.92. As a result, the peak wavelength shifts to 1585 nm, and the peak efficiency reduces to -6.2dB even when the fiber is tilted to 20°, according to the simulation result shown by the red curve in Figure S5d. However, the experimental results demonstrate a better efficiency of -5.2 dB, and the peak wavelength shifts back to 1545 nm. It is possibly due to the fact that the holes of subwavelength structures become larger when they are filled with SU-8, which leads to a smaller effective refractive index and therefore the peak wavelength shifts to shorter wavelengths. To sum up, the grating demonstrates satisfying performance with and without SU-8 fillings. Although the peak wavelength shifts about 30 nm, the wavelength range of interest is still covered due to the large bandwidth of the grating coupler.

To assure the grating is functional while being bent, the performance of the grating coupler under different bending conditions is also characterized, as shown in Figure S6. The sample under investigation is the grating filled with SU-8. The input and output fibers are tilted at a fixed angle of 20°. Figure S6a shows the shift of peak wavelength under bending along longitudinal direction. For longitudinal face-out (LFO) bending, the peak wavelength shifts to longer wavelength, while for longitudinal face-in (LFI) bending the peak wavelength shifts to shorter wavelength. It is experimentally observed that the efficiency of grating couplers is not affected by bending. Since the coupling efficiency heavily depends upon the effective index, a relatively stable coupling efficiency indicates that the subwavelength structure has negligible deformation, otherwise the coupling efficiency should show significant decrease. This assertion matches the mechanical simulation, which shows that the maximum strain is around 1%, corresponding to only about 7 nm variation in the period. Thus, we can assume that the shift of the peak wavelength is mainly caused by the change of the relative coupling angle. As shown by the cartoon in Figure S6a, the coupling angle reduces along with the bending radius. According to the phase matching condition:

$$\frac{2\pi n_{neffavg}}{\lambda} = \frac{2\pi n_c \sin\theta_o}{\lambda} + \frac{2\pi}{\Lambda} \tag{S-1}$$

The peak wavelength $\lambda_0$can be calculated by:

$$\lambda_0 = \Lambda\left(n_{neffavg} - n_c \sin\theta_o\right) \tag{S-2}$$

Here, Λ is the grating period. $n_{neffavg}$ is the average effective index of the grating coupler. n_c is the refractive index of the cladding, which equals to 1. θ_0 represents the fiber tilting angle, which can be estimated by approximately considering the bending curvature as part of a circle. The red curves in Figure S6b and c are the simulation results, which matches the experimental data. Similarly, for transverse face-out (TFO) and transverse face-in (TFI) bending, shown in Figure S6d~e, the peak wavelength of the grating coupler stays the same due to the fact that the bending does not change any of the parameters in the phase matching condition. The discrepancy is from the fact that the device cannot be precisely placed on the top of the curvature.

4. Mechanical Analysis

As mechanics and photonics have different conventions on coordinates, to avoid potential ambiguities, the coordinate system needs to be clarified prior to analysis. In this paper, we define the light propagation direction as z axis. In the device plane, the direction perpendicular to the light propagation direction is defined as x axis. The out of plane direction is y axis. The device is fabricated along <110> crystal direction, and thus x and z axis are along <110> crystal direction and y axis is along <100> crystal direction.

As indicated by Figure S7a, the film comprises of three layers, a 250 nm thick silicon device layer, a ~3 μm thick SU-8 layer, and a 125 μm thick Kapton film. Conducting a complete analysis on the mechanical and optical properties of the deformed photonic crystal cavity in 3D space demands unrealistically long time. Alternatively, we first exploit plane strain model in the yz plane for longitudinal bending (or xz plane for transverse bending) to estimate the bending-induced strain of the silicon nanomembrane, and then use plane stress model in the xz plane with prescribed strain boundary condition obtained from the bending analysis to simulate the deformation of the photonic crystal cavity.

Subjecting the film to a compressive force causes it buckle (Figure S7b) and the bent shape can be described by the following sinusoidal curve: [12, 13]

$$w = w_0 \sin\left(\frac{\pi D}{L - \Delta L}\right) \tag{S-3}$$

w_0 is the deflection of the specimen at the center of the specimen. It is defined as:

$$w_0 = \frac{2}{\pi} L \sqrt{\frac{\Delta L}{L} - \frac{\pi^2 h^2}{12 L^2}} \tag{S-4}$$

D=z for bending along z direction (longitudinal bending), and D=x for bending along x direction (transverse bending). $w$and h denote the deflection of the specimen in y direction and the total thickness of the specimen (a summation of the thickness of the silicon layer h_1, the thickness of the SU-8 layer h_2, and the thickness of the Kapton film h_3), respectively. The second term under the square root can be dropped because h (125 μm) is much smaller than the length of the specimen L (30 mm). The bending radius at the center of the specimen can be estimated by: [12]

$$R = \frac{L}{2\pi\sqrt{\frac{\Delta L}{L}}} \tag{S-5}$$

The strain on the top surface can be calculated by dividing its distance to the neutral plane by the bending radius. The position of the neutral plane can be calculated through [14]:

$$d = \frac{\sum_{i=1}^{3} \overline{E_i} h_i d_i}{\sum_{i=1}^{3} \overline{E_i} h_i} \tag{S-6}$$

Here, $\bar{E}_i = E_i/(1-v_i^2)$, representing the plane strain modulus. E_i is the Young's modulus, and v_i is Poisson's ratio. h_i denotes the thickness of the i-th layer. The Young's moduli and Poisson's ratios of the involved materials are listed in Table S1. d_i is the distance between the middle plane of the i-th layer to the bottom of the specimen as denoted in Figure S7A. It has been proved that patterned silicon nanomembranes bonded to Kapton substrates have very similar strains (excluding the edge effect) to their blanket counterpart because of the small elastic mismatch [15]. Since the patterned area is very small and the microcavities only cover a small fraction of the area, the effective Young's modulus of the patterned nanomembrane can be assumed to be close to the Young's modulus of silicon. On the top surface, the strain in the bending direction γ_{bend} can be calculated by:

$$\gamma_{bend} = \frac{h-d}{R} \tag{S-7}.$$

The relation between the bending radius and the strain is illustrated by the curve shown in Figure S8. Eq. (S-7) implies that the strain of silicon nanomembrane could be tuned by adjusting the position of the neutral plane. For example, when $h = d$, the strain induced by bending is negligible and the film could be bended to an extremely small curvature.

The strain γ_{bend} calculated from (S-7) is applied in the 2D plane stress finite element modeling by specifying displacement boundary conditions at the left and right ends. For longitudinal bending (bending in z direction), $\gamma_{zz} = \gamma_{bend}$; for transverse bending (bending in x direction), $\gamma_{xx} = \gamma_{bend}$. Since the dimension of the cavity is much smaller than the bending radius, and also the light propagates along the bending curvature, the in-plane 2D stretching and compressing is a close approximation to bending in 3D space. The deformation of the holes is simulated by finite-element-method (FEM) using commercial software COMSOL. Due to the nonuniformly distributed holes, the stress distribution is not uniform. Hence, here, an averaged stress over the whole 2D domain is used for the finite-difference time-domain (FDTD) simulations.

5. Bending Induced Photo-elastic Effect

As indicated in Figure S8, bending can induce more than 1% of strain, which corresponds to stress as high as one GPa. The refractive index change caused by stress is larger than 0.01.[16] According to reference [17], a small perturbation of the refractive index is sufficient to cause a shift

of the resonance as the mode is confined inside the high index silicon nanomembrane. The frequency shift Δf could be evaluated by

$$\Delta f = \left(\frac{1}{1+\frac{\eta \Delta n}{n}} - 1 \right) f_0 \tag{S-8}$$

for small index change $\Delta n/n$. η is the fraction of mode field confined inside the high index region. f_0 represents the resonance frequency. Assuming η equals to 0.85, a change of 0.01 could result in a resonance wavelength shift of around 4 nm. Thus, the photo-elastic effect must be taken into consideration.

In our specific case, the strain could be written as: [18]

$$\gamma = \begin{pmatrix} \gamma_{xx} & \gamma_{xy} & \gamma_{xz} \\ \gamma_{xy} & \gamma_{yy} & \gamma_{yz} \\ \gamma_{xz} & \gamma_{yz} & \gamma_{zz} \end{pmatrix} \tag{S-9}$$

Due to the symmetry, there are six independent elements. Since the shear force has negligible effects on the optical performance, γ_{xy}, γ_{xz}, and γ_{yz} can be ignored. [16] Thus, the strain tensor is simplified into

$$\gamma = \begin{pmatrix} \gamma_{xx} & 0 & 0 \\ 0 & \gamma_{yy} & 0 \\ 0 & 0 & \gamma_{zz} \end{pmatrix} \tag{S-10}$$

The dielectric tensor takes the form of [18]

$$\varepsilon = \begin{pmatrix} n_{xx}^2 & n_{xy}^2 & n_{xz}^2 \\ n_{xy}^2 & n_{yy}^2 & n_{yz}^2 \\ n_{xz}^2 & n_{yz}^2 & n_{zz}^2 \end{pmatrix} \tag{S-11}$$

For cubic crystals like silicon, the dielectric tensor can be simplified into:

$$\varepsilon = \begin{pmatrix} n_{xx}^2 & 0 & 0 \\ 0 & n_{yy}^2 & 0 \\ 0 & 0 & n_{zz}^2 \end{pmatrix} \tag{S-12}$$

This strain-optic coefficient of this type of crystal can be written as [16] :

$$p=\begin{pmatrix} p_{11} & p_{12} & p_{12} & 0 & 0 & 0 \\ p_{12} & p_{11} & p_{12} & 0 & 0 & 0 \\ p_{12} & p_{12} & p_{11} & 0 & 0 & 0 \\ 0 & 0 & 0 & p_{44} & 0 & 0 \\ 0 & 0 & 0 & 0 & p_{44} & 0 \\ 0 & 0 & 0 & 0 & 0 & p_{44} \end{pmatrix} \tag{S-13}$$

For silicon, p_{11}=-0.101, and p_{12}=0.0094. The relation between the refractive index and the strain is governed by:

$$\Delta\begin{pmatrix} 1/n_{xx}^2 \\ 1/n_{yy}^2 \\ 1/n_{zz}^2 \\ 1/n_{yz}^2 \\ 1/n_{xz}^2 \\ 1/n_{xy}^2 \end{pmatrix}=\begin{pmatrix} p_{11} & p_{12} & p_{12} & 0 & 0 & 0 \\ p_{12} & p_{11} & p_{12} & 0 & 0 & 0 \\ p_{12} & p_{12} & p_{11} & 0 & 0 & 0 \\ 0 & 0 & 0 & p_{44} & 0 & 0 \\ 0 & 0 & 0 & 0 & p_{44} & 0 \\ 0 & 0 & 0 & 0 & 0 & p_{44} \end{pmatrix}\begin{pmatrix} \gamma_{xx} \\ \gamma_{yy} \\ \gamma_{zz} \\ 0 \\ 0 \\ 0 \end{pmatrix} \tag{S-14}$$

Obviously, $\Delta(1/n_{yz}^2)$, $\Delta(1/n_{xz}^2)$, and $\Delta(1/n_{xy}^2)$ are zero due to the fact that the shear strain has been ignored in the discussion. Therefore, the equation turns into

$$\Delta\begin{pmatrix} 1/n_{xx}^2 \\ 1/n_{yy}^2 \\ 1/n_{zz}^2 \end{pmatrix}=\begin{pmatrix} p_{11} & p_{12} & p_{12} \\ p_{12} & p_{11} & p_{12} \\ p_{12} & p_{12} & p_{11} \end{pmatrix}\begin{pmatrix} \gamma_{xx} \\ \gamma_{yy} \\ \gamma_{zz} \end{pmatrix} \tag{S-15}$$

With the stress-strain relation: [19]

$$\gamma_{xx}=\frac{1}{E_{xx}}[\sigma_{xx}-\nu(\sigma_{yy}+\sigma_{zz})] \tag{S-16}$$

$$\gamma_{yy}=\frac{1}{E_{yy}}[\sigma_{yy}-\nu(\sigma_{xx}+\sigma_{zz})] \tag{S-17}$$

$$\gamma_{yy}=\frac{1}{E_{yy}}[\sigma_{yy}-\nu(\sigma_{xx}+\sigma_{zz})] \tag{S-18}$$

The relation between the stress and refractive index is:

$$\begin{pmatrix} n_{xx} \\ n_{yy} \\ n_{zz} \end{pmatrix}=\begin{pmatrix} n_0 \\ n_0 \\ n_0 \end{pmatrix}-\begin{pmatrix} C_1 & C_2 & C_2 \\ C_2 & C_1 & C_2 \\ C_2 & C_2 & C_1 \end{pmatrix}\begin{pmatrix} \sigma_{xx} \\ \sigma_{yy} \\ \sigma_{zz} \end{pmatrix} \tag{S-19}$$

Here,

$$C_1 = \frac{n_0^3}{2}\left[\frac{p_{11}}{E_{xx}} - \frac{p_{12}}{E_{yy}}\upsilon - \frac{p_{12}}{E_{zz}}\upsilon\right] \quad \text{(S-20)}$$

$$C_2 = \frac{n_0^3}{2}\left[-\frac{p_{11}}{E_{xx}}\upsilon + \frac{p_{12}}{E_{yy}} - \frac{p_{12}}{E_{zz}}\upsilon\right] \quad \text{(S-21)}$$

C_1 and C_2 are -13.3×10^{-12} Pa^{-1} and 4.7×10^{-12} Pa^{-1}, respectively. The average stress and induced change of refractive index are shown in Figure S9. The average stress versus strain, and refractive index versus strain appears to have a linear correlation.

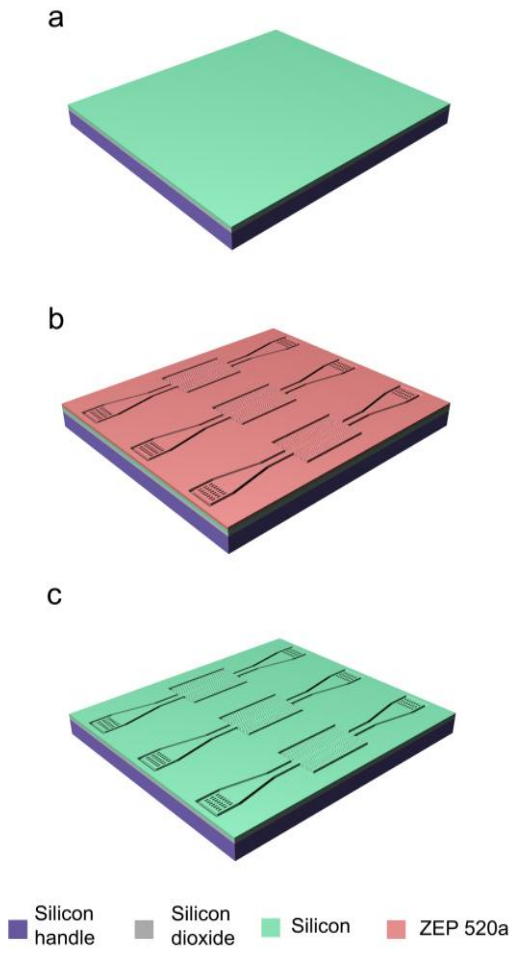

Figure S1.

Pattern SOI into L13 Cavity. a. SOI chip with 250 nm silicon, 3 μm BOX and 675 μm silicon handle. b. Pattern electron beam resist layer. c. Transfer the pattern onto silicon device layer with RIE.

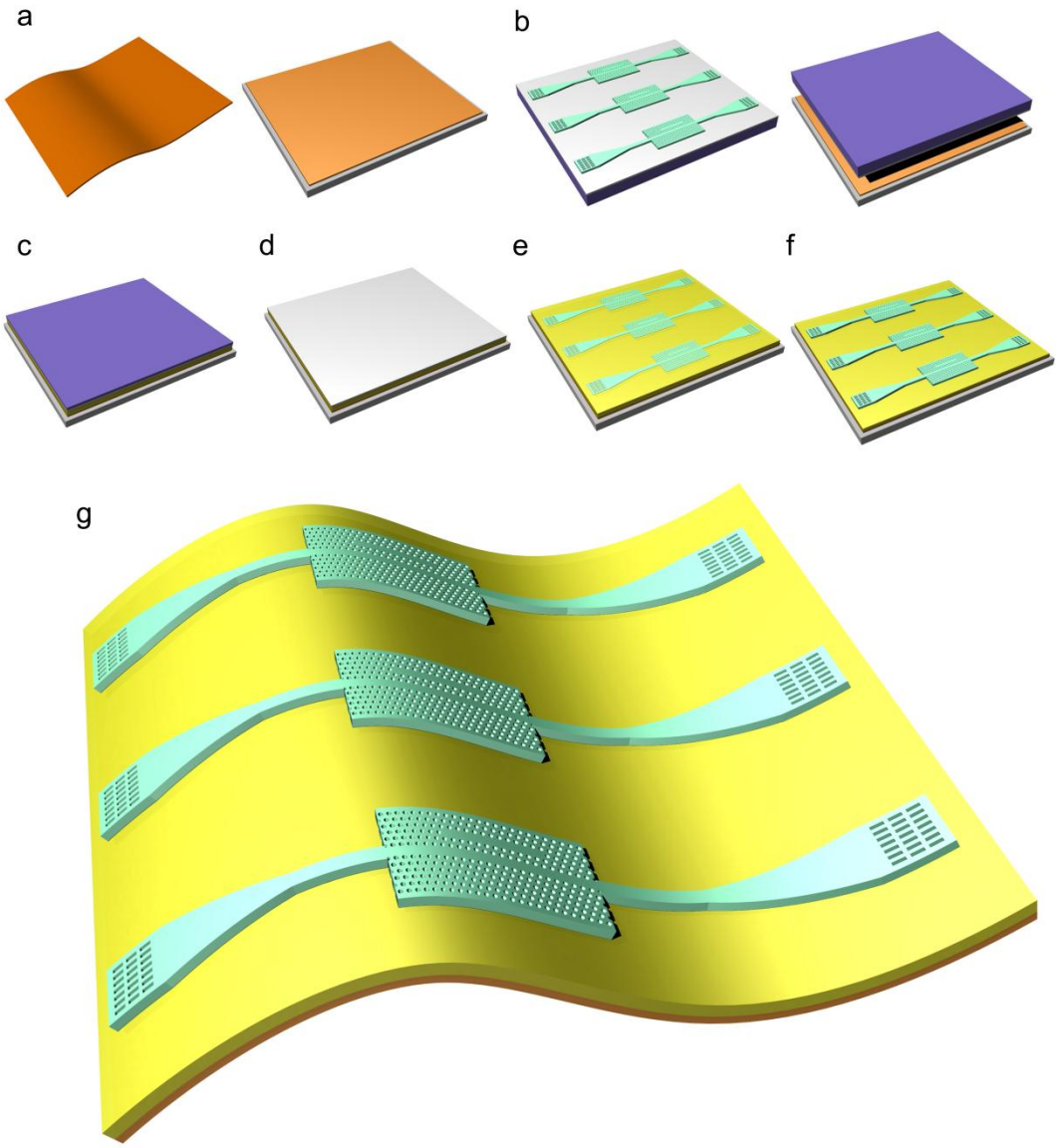

Figure S2

Tranfer Process. a. Clean and mount a Kapton film on a silicon chip. b. Fabricate L13 PC microcavity devices with integrated SWG couplers on SOI, flip over and bond the chip onto the Kapton film with SU-8 as adhesive layer. c. Thin down the silicon handle to ~ 100 μm using mechanical polishing. d. Use deep silicon etching to etch away the remaining ~ 100 μm silicon. e. Remove the box layer with HF. f. Remove the SU 8 filled into the holes of photonic crystal to enhance the sensitivity. g. Peel off the Kapton film.

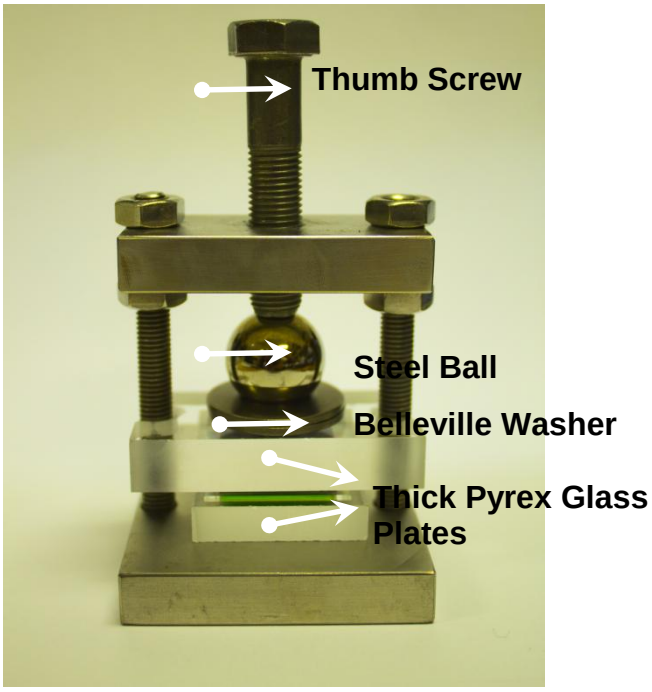

Figure S3

The home-made bonder. The samples to be bonded are mounted between two thick Pyrex glass plates. The pressure is controlled via a thumb screw, a steel ball and Belleville washer.

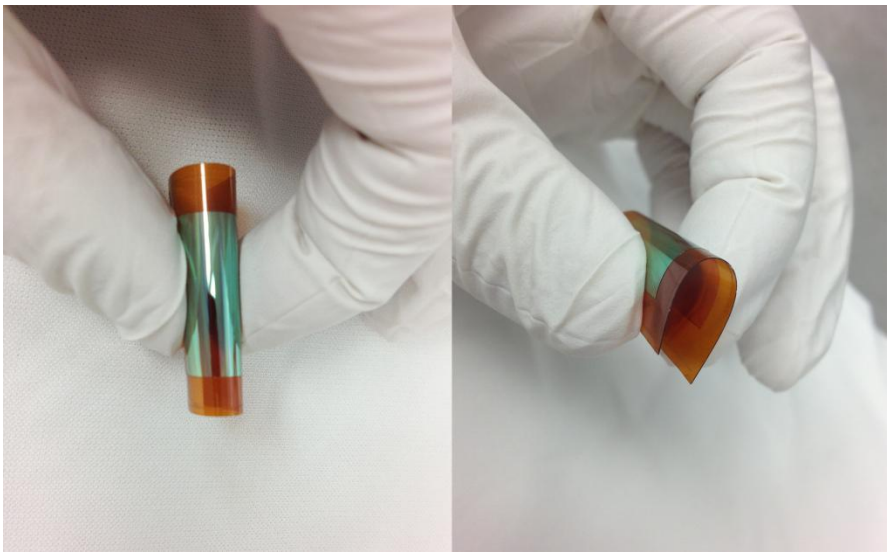

Figure S4

Silicon nanomembrane transferred onto Kapton film. The transferred nanomembrane can be bent to a very small radius without breaking or cracking the film.

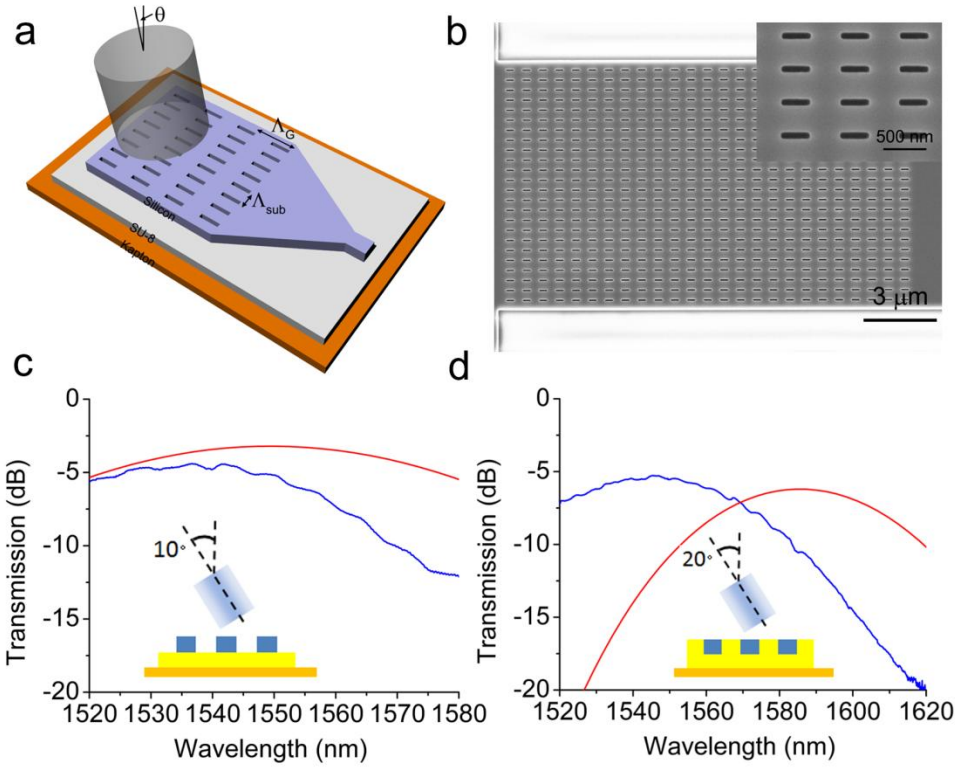

Figure S5

a. schematic of the subwavelength grating coupler. b. SEM images of the grating coupler. Inset: the enlarged view of the subwavelength grating coupler. The simulation and experimental results of subwavelength grating couplers after transfer. c. the holes are not filled with SU-8. d. the holes are filled with SU-8. Red: simulation curve. Blue: experimental results.

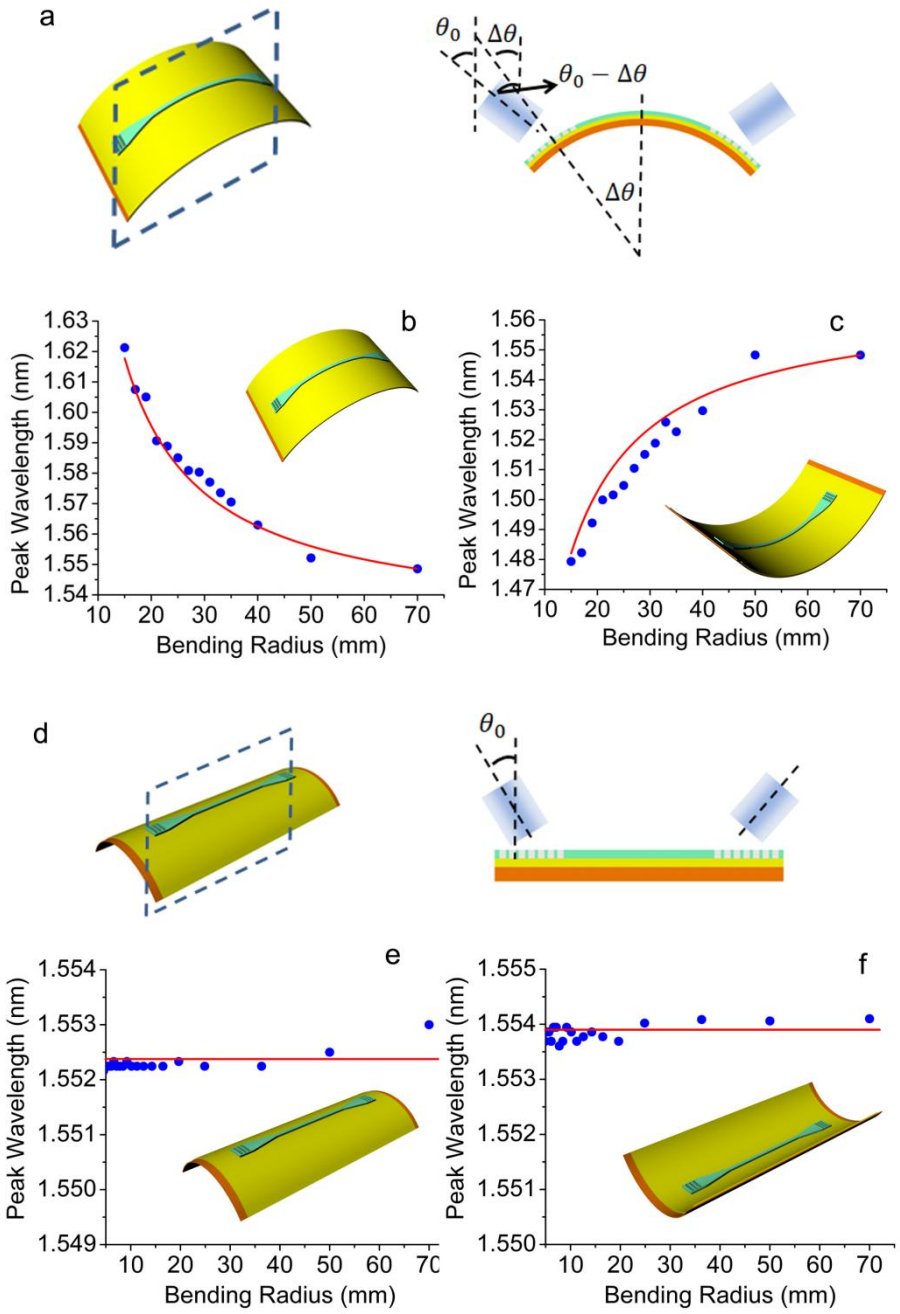

Figure S6

Peak wavelength shift of grating couplers under different bending conditions. a. schematic of the longitudinal bending. b. longitudinal face-out bending. c. longitudinal face-in bending. d. schematic of the transverse bending. e. transverse face-out bending. f. transverse face-in bending.

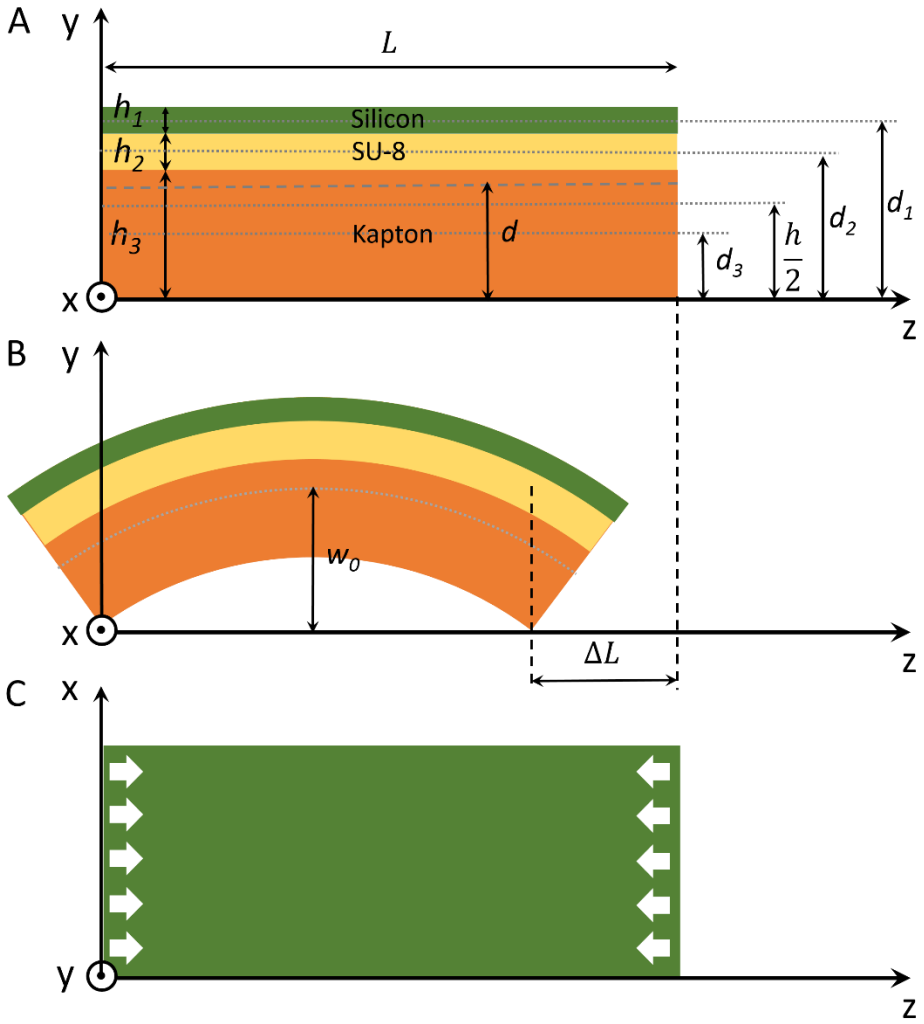

Figure S7
Schematics for the 2D simulation models. (A)(B) The mechanical model in the yz plane. h_i (i=1,2,3)- the thickness of silicon, SU-8, and Kapton; d_i (i=1,2,3)- the position of the middle planes of silicon, SU-8, and Kapton; d- mechanic neutral plane; h- the total thickness of the sample ($h=h_1+h_2+h_3$); (C) The deformation of the device in xz plane is simulated by applying the strain estimated from the bending in yz plane.

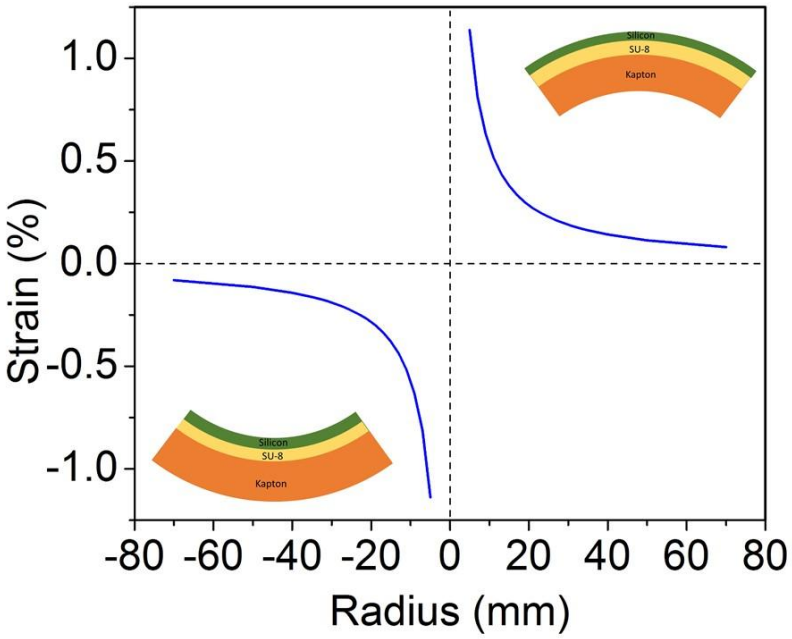

Figure S8
The strain of the silicon nanomembrane in relation to the bending radius. The maximum strain achieved is around 1% for our configuration.

Table S1.

Material characteristics and thickness

Material	Young's Modulus (GPa)	Poisson's Ratio	Thickness (μm)
Si <110>	169	0.28	0.25
Si <100>	130		
SU-8	2	0.22	3
Kapton	2.5	0.34	125

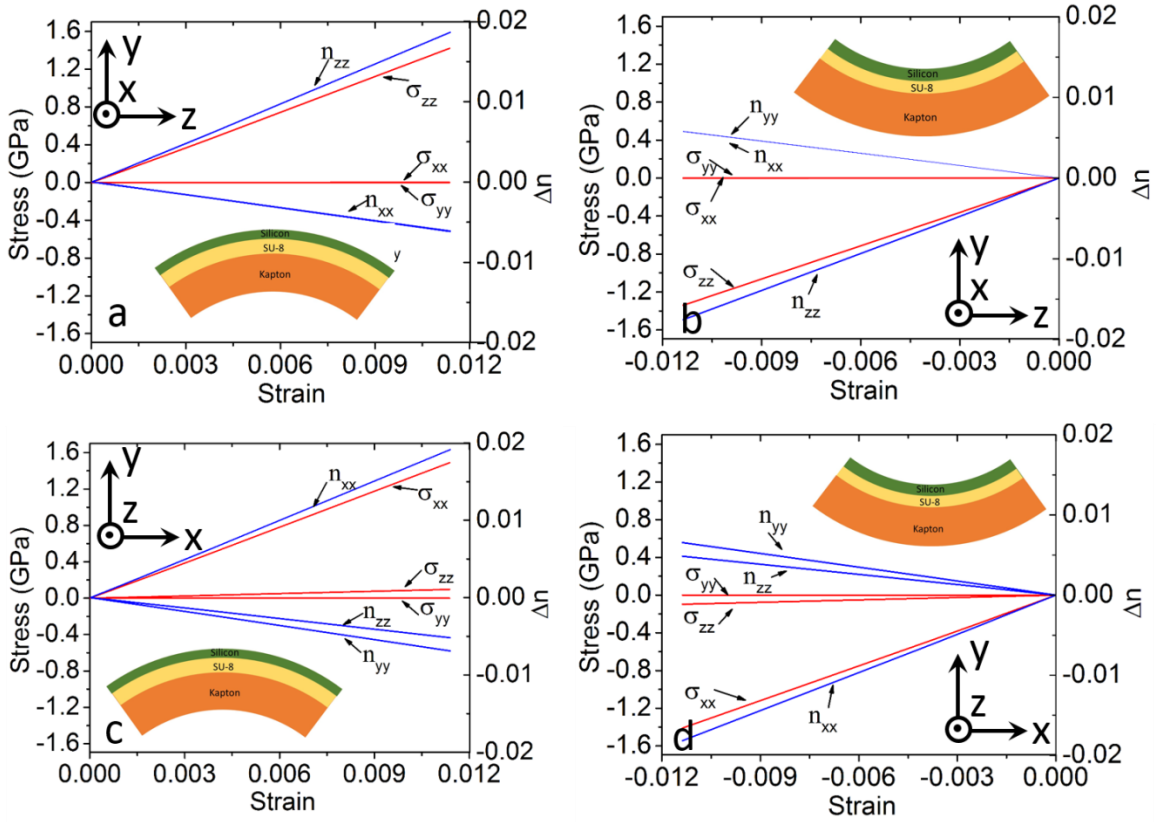

Figure S9.

The averaged stress and the photo-elastic effect induced refractive index variation. a. longitudinal face-out bending. b. transverse face-out bending. c. longitudinal face-in bending. d. transverse face-in bending.

Movie S1

Flexible single-crystal silicon nanomembrane based photonic crystal microcavity

Reference

1. Pfeiffer, K.; Fink, M.; Gruetzner, G.; Bleidiessel, G.; Schulz, H.; Scheer, H. Multistep Profiles by Mix and Match of Nanoimprint and UV Lithography. *Microelectron. Eng.* **2001**, 57–58, 381-387.
2. Santeri, T.; Sami, F. Wafer-Level Bonding of MEMS Structures with SU-8 Epoxy Photoresist. *Phys. Scr., T* **2004**, *114*, 223-226.
3. Madou, M. J. Fundamentals of Microfabrication and Nanotechnology. 3rd ed.; CRC press: 2011.
4. Xu, X. C.; Subbaraman, H.; Hosseini, A.; Lin, C. Y.; Kwong, D.; Chen, R. T. Stamp Printing of Silicon-Nanomembrane-Based Photonic Devices onto Flexible Substrates with a Suspended Configuration. *Opt. Lett.* **2012**, *37*, 1020-1022.
5. Taillaert, D.; Van Laere, F.; Ayre, M.; Bogaerts, W.; Van Thourhout, D.; Bienstman, P.; Baets, R. Grating Couplers for Coupling between Optical Fibers and Nanophotonic Waveguides. *Jpn. J. Appl. Phys.* **2006**, *45*, 6071-6077.
6. Tang, Y. B.; Wang, Z.; Wosinski, L.; Westergren, U.; He, S. L. Highly Efficient Nonuniform Grating Coupler for Silicon-on-Insulator Nanophotonic Circuits. *Opt. Lett.* **2010**, *35*, 1290-1292.
7. Roelkens, G.; Vermeulen, D.; Van Thourhout, D.; Baets, R.; Brision, S.; Lyan, P.; Gautier, P.; Fedeli, J. M. High Efficiency Diffractive Grating Couplers for Interfacing a Single Mode Optical Fiber with a Nanophotonic Silicon-on-Insulator Waveguide Circuit. *Appl. Phys. Lett.* **2008**, *92*, 131101.
8. Xu, X. C.; Subbaraman, H.; Covey, J.; Kwong, D.; Hosseini, A.; Chen, R. T. Complementary Metal-Oxide-Semiconductor Compatible High Efficiency Subwavelength Grating Couplers for Silicon Integrated Photonics. *Appl. Phys. Lett.* **2012**, *101*, 031109.
9. Halir, R.; Cheben, P.; Schmid, J. H.; Ma, R.; Bedard, D.; Janz, S.; Xu, D. X.; Densmore, A.; Lapointe, J.; Molina-Fernandez, I. Continuously Apodized Fiber-to-Chip Surface Grating Coupler with Refractive Index Engineered Subwavelength Structure. *Opt. Lett.* **2010**, *35*, 3243-3245.
10. Chen, X.; Tsang, H. K. Nanoholes Grating Couplers for Coupling between Silicon-on-Insulator Waveguides and Optical Fibers. *IEEE Photon. J.* **2009**, *1*, 184-190.
11. Yeh, P.; Yariv, A.; Hong, C. S. Electromagnetic Propagation in Periodic Stratified Media .1. General Theory. *J. Opt. Soc. Am.* **1977**, *67*, 423-438.
12. Park, S. I.; Ahn, J. H.; Feng, X.; Wang, S. D.; Huang, Y. G.; Rogers, J. A. Theoretical and Experimental Studies of Bending of Inorganic Electronic Materials on Plastic Substrates. *Adv. Funct. Mater.* **2008**, *18*, 2673-2684.
13. Timoshenko, S. P.; Gere, J. M. Theory of Elastic Stability. 2nd ed.; Dover Publications: 2009.
14. Bareisis, J. Stiffness and Strength of Multilayer Beams. *J Compos Mater* **2006**, *40*, 515-531.
15. Yang, S. X.; Lu, N. S. Gauge Factor and Stretchability of Silicon-on-Polymer Strain Gauges. *Sensors* **2013**, *13*, 8577-8594.
16. Huang, M. Stress Effects on the Performance of Optical Waveguides. *Int. J. Solids. Struct.* **2003**, *40*, 1615-1632.
17. Fan, S. Photonic Crystals: Theory and Device Applications. Massachusetts Institute of Technology, 1997.

18. Chen, Y.; Li, H.; Li, M. Flexible and Tunable Silicon Photonic Circuits on Plastic Substrates. *Sci Rep* **2012**, *2*, 622.
19. Sadd, M. H. Elasticity Theory, Applications, and Numerics. 2nd ed.; Academic Press: 2009.